Review article

Artem S. Polushkin, Ekaterina Y. Tiguntseva, Anatoly P. Pushkarev and Sergey V. Makarov*

Single-particle perovskite lasers: from material properties to cavity design

https://doi.org/10.1515/nanoph-2019-0443
Received October 25, 2019; revised December 4, 2019; accepted December 5, 2019

Abstract: Last decade, halide perovskites demonstrate high potential for efficient, tunable, and cheap photonic sources. Recently, single-particle perovskite lasers of various compositions and shapes with all dimensions close or smaller than the emitted wavelengths were demonstrated experimentally in a broad range of temperatures. In this review, we aim to cover not only the recent progress in the single-particle perovskite lasers but also provide a comprehensive analysis on strategies to achieve the most compact perovskite lasers with the best working parameters.

Keywords: halide perovskites; nanoparticles; nanolasers and microlasers; optical resonances; semiconductors.

1 Introduction

The history of halide perovskite started in 1893, when Wells [1] first synthesized cesium lead halide perovskite, while halide perovskites with organic cation (e.g. $MA = CH_3NH_3^+$) were synthesized in 1978 only [2], as shown in Figure 1A. By the end of 1990-s century, the basic optical and electronic properties were studied by David Mitzi [18] mostly and by other groups [19, 20]. However, only after demonstration of the first $MAPbI_3$-based solar cell in 2009 by Miyasaka's group [3] that lead halide perovskites have been considered as one the most prospective materials for various optoelectronic applications: photovoltaics [21] and light-emitting diodes [22]. Indeed, they possess strong and tunable interband transitions in the entire visible range competing with the best standard semiconductors such as GaAs. As a result, the first perovskite-based lasers appeared in 2014 [4, 23], while continuous-wave optically pumped perovskite lasers were demonstrated in 2017 [5].

Parallel to the progress in the halide perovskites, new "laser era" raised after the first laser was invented by Maiman [6] in 1960, resulting in the development of semiconductor-based lasers after the demonstration of the first prototype in 1970 operating at room temperature [7]. Further progress of semiconductor lasers developing was size decreasing to overcome diffraction limits and to create ever smaller lasers [24–32].

In this general trend in laser physics and technologies, the compactization of perovskite-based lasers is one of the most rapidly developing directions. Figure 1B shows the milestones in the progress of development of single-particle perovskite lasers from relatively large microplate (MPL)-based two-dimensional (2D) design [8] to nanowires (1D design) [15] and eventually to such 0D designs as nanospheres [16] and nanocubes [17]. Current record-small perovskite nanolasers have already achieved the volumes less than the volume of emitted photons in free space [17, 33]. Because further progress in this field would require even stronger light confinement in a single nanoparticle, it is highly important to understand what is the ultimate size limit for perovskite-based single-particle lasers. Figure 2 shows the most important parameters for laser size minimization. In this focused review, we aim to discuss the impact of material and cavity properties on lasing from single-particle lasers based on the halide perovskites.

***Corresponding author: Sergey V. Makarov,** Department of Physics and Engineering, ITMO University, St. Petersburg 197101, Russia, e-mail: s.makarov@metalab.ifmo.ru. https://orcid.org/0000-0002-9257-6183
Artem S. Polushkin and Anatoly P. Pushkarev: Department of Physics and Engineering, ITMO University, St. Petersburg 197101, Russia
Ekaterina Y. Tiguntseva: Department of Physics and Engineering, ITMO University, St. Petersburg 197101, Russia; and Far Eastern Federal University, Vladivostok 690041, Russia

2 Perovskite light-emitting properties

2.1 Some advantages of perovskites

In this review, we focus on 3D halide perovskites family of materials with formula ABX_3, where "A" is the cation

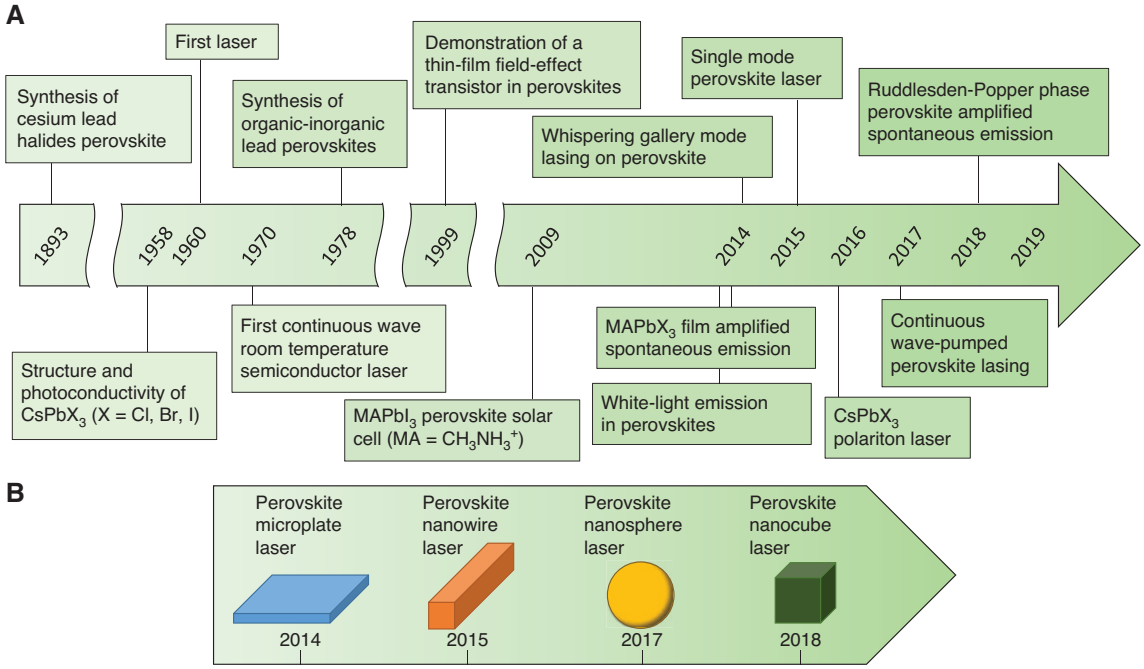

Figure 1: History of lasers based on halide perovskites.
(A) General milestones from halide perovskite synthesis to the application for lasers [1–14]. (B) Evolution of single-particle perovskite lasers [8, 15–17].

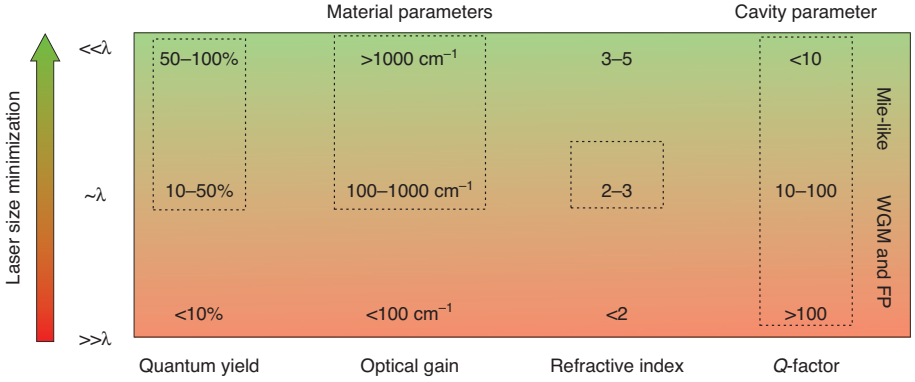

Figure 2: Scheme for the most important parameters for laser size minimization.
Dashed lines indicate ranges of values typical for bulk halide perovskites.

(e.g. MA^+, FA^+, or Cs^+), "B" is usually lead (Pb^{2+}), and "X" is the anion (e.g. I^-, Br^-, or Cl^-). Halide lead perovskites can be considered as direct band-gap materials resembling GaAs. But they have some advantages that make them a very perspective material for nanophotonics. One of such advantages is high optical gain being higher than 10^3 cm^{-1} at room temperature owing to strong interband transition [34]. Moreover, the halide perovskites have denominated exciton at room temperature with electron–hole binding energy up to 100 meV [35–40]. High defect tolerance allows achieving photoluminescence (PL) even with defect concentration 10^{17} cm^{-3} [41]. One of the most important advantages of halide perovskite is capability to tune band-gap size by chemical method in the range 1.7–3 eV [42, 43]. Another reason why the halide perovskites are so popular materials for photovoltaics and photonics is their cost-efficiency governed by simple wet chemistry methods of fabrication and earth abundance of all components [44]. Regarding additional optical outstanding properties, perovskites possess high nonlinear absorption coefficients. For example, $CsPbBr_3$ perovskite has three-photon and two-photon absorption coefficients

0.14 ± 0.03 cm^3 GW^{-2} at 1200 nm [45] and 4.57 cm GW^{-1} at 800 nm [46], respectively. Comparing GaAs has 26 cm GW^{-1} at 1060 nm and 0.35 ± 0.05 cm^3 GW^{-2} at 1680 nm [47], GaN has 6.35×10^{-3} cm GW^{-1} at 410 nm and 1.05×10^{-10} cm^3 GW^{-2} at 820 nm [48] two- and three-photon absorption coefficients, respectively. These properties enabled demonstrations of multiphoton excitation of various perovskite-based microlasers [46, 49–51] Nevertheless, perovskites have some disadvantages as degradation at atmosphere due to interaction with water and oxygen, light-induced phase segregation, reaction with metals (Au, Ag), and parasitic migration of ions and defects, as well as low thermal conductivity around 0.5 W m^{-1} K^{-1} [43, 52]. These factors limit the realization of perovskite-based electrically pumped lasers [53]. Therefore, material and cavity properties optimization has crucial importance for further development of this direction.

2.2 Photoluminescence

The quality of emitting semiconductor can be assessed from the kinetics of generated charge carriers relaxation. The kinetics of generation and relaxation of free carriers in halide perovskites are usually described with the following general equation:

$$\frac{dN_{fc}}{dt} = G - (R_{\text{rad}} + R_{\text{nrad}}), \tag{1}$$

where G is the photoexcited carriers generation rate; R_{rad} is the recombination rate caused by spontaneous light emission; and R_{nrad} is the recombination rate usually associated with trap-assisted recombination that relies on an individual carrier (electron or hole) being captured in a trap. Also, Auger recombination (cubic term of N_{fc}) should be taken into account at very high densities ($N_{fc} > 10^{18}$ cm^{-3}). The radiative relaxation term corresponds to intrinsic electron–hole recombination, which depends on both electron and hole densities and thus has quadratic dependence on N_{fc}. As a result, the internal quantum yield (QY) can be written as follows:

$$QY = \frac{R_{\text{rad}}}{R_{\text{rad}} + R_{\text{nrad}}} \tag{2}$$

Remarkably, that main negative contribution to QY in real semiconductor nanostructures comes from nonradiative Shockley–Read–Hall recombination mechanism with the rate $R_{\text{SRH}} = N_T N_{fc}(K_n + K_p)/2$, where K_n and K_p are kinetic factors that encompass both the trap capture cross section and thermal velocity of the electrons and holes, respectively, and N_T is the trap state density. In the halide perovskites, even high trap state density ($N_T \sim 10^{14}$–10^{17} cm^{-3}) usually yields relatively weak contribution to QY because of the low formation energy defects in perovskites residing near the band edges, which render the lead-halide perovskite semiconductors tolerant to defects. More detailed analysis with taking into account recycling, polaron, and Rashba effects is presented in [54, 55].

Shifting PL spectra to blue or red region is possible with mixed-halide $CsPbBr_{3-x}Cl_x$ and $CsPbBr_{3-x}I_x$ compositions. However, mixing anions in perovskites, one inevitably sacrifices QY because of the higher trap state density in the forming materials [see Discussion for (2)] [56] and hence increases F_{th} as well as decreases the quality factor of lasing modes [57].

One can also derive from (2) the expression for temperature dependence of QY on taking into account the emission from an excitonic state:

$$QY(T) = \frac{1}{1 + Ue^{-E_b/k_B T}} \tag{3}$$

in which U is the coefficient containing the ratio between radiative and nonradiative relaxation rates, which is a function of N_{fc}; E_b is the binding energy of exciton being dependent on T for the halide perovskites [38, 58], and k_B is the Boltzmann constant. In order to quantify the lasing threshold properties relatively, the pump threshold is usually fitted by the exponential dependence on temperature relation [59]:

$$F_{th}(T) = F_{th,0} e^{\frac{T}{T_0}} \tag{4}$$

where $F_{th,0}$ is the threshold pump fluence at low temperature, and T_0 is the characteristic temperature, which is used to signify the strength of PL temperature dependence. For example, single-crystal $CsPbBr_3$ microparticles have relatively high characteristic temperatures $T_0 \approx 300$ K [46], which is larger than the typical T_0 around 100 K of bulk or quantum well-based lasers [60]. Such relatively weak temperature sensitivity opens the way for room-temperature ultracompact lasers. On the other hand, the temperature-dependent PL experiments for polycrystalline films of $MAPbI_3$ were fitted by much lower characteristic temperature, $T_0 \approx 75$ K [53], which was attributed to the significant role of defects.

2.3 Lasing

First, we should discuss the nature of lasing in lead halide perovskite single-particle cavities. Generally, there are two

main mechanisms of lasing discussed in the literature: from electron–hole pair emission [61] or from exciton–polaritons Bose condensation [62, 63]. However, it was revealed recently that the threshold carrier density for lasing in the single-particle perovskite designs is usually above the Mott-transition critical density, which most likely results in stimulated emission of electron–hole plasma rather than the Bose condensation of exciton–polaritons [64].

In order to discuss the main contributions to lasing performance of perovskite-based nanocavities, let us consider basic equations for kinetics of carriers (N_{fc}) and photons (s) in a laser mode:

$$\frac{dN_{fc}}{dt} = G - (R_{\text{nrad}} + R_{sp}) - v_g g s, \tag{5}$$

$$\frac{ds}{dt} = \Gamma g v_g s - s/\tau_p + \Gamma \beta R_{sp} \tag{6}$$

where G is the generation rate; R_{sp} is the recombination rate associated with spontaneous emission; v_g is group velocity of light in the medium; s is the number of photons in the mode; g is the material gain; Γ is the coupling factor for the mode with the active media; β is the part of spontaneous emission that couples into the lasing mode; $\tau_p = Q_{\text{cavity}}/\omega$ is the photon lifetime within the cavity.

We would like to stress two main contributions to the lasing threshold:

(i) Quality factor (Q_{cavity}) of a cavity, determining the lifetime of photons in the laser mode and governed both by dissipative losses in the material and by radiative losses in the cavity. Thus, assuming that the material losses are compensated by pump, one can derive from (6) the condition for the minimal radiative part of cavity Q_{cavity} factor required for lasing:

$$Q_{th} = \frac{\omega}{v_g \Gamma g_{th}}, \tag{7}$$

where g_{th} is the threshold material gain. Keeping in mind that the gain g is a function of N_{fc}, in the most optimal case, one has to achieve a certain level of gain at the lowest generation rate (G).

(ii) The minimization of G requires high values of QY, which is governed by nonradiative recombination (R_{nrad}). This contribution is strongly connected with deep-level defects concentration in the material. Thus, one can see from (5) that minimization of R_{nrad} would give the highest carriers concentration at given G. The minimization of pumping intensities or current densities is crucial for avoiding nanolaser overheating.

Therefore, we will analyze the contributions both from cavity design and material quality in order to discuss the strategy for the creation of ultimately compact perovskite-based lasers.

3 Perovskite cavities properties

3.1 Nanoparticles subwavelength in all dimensions: Mie resonances

Optical modes in the dielectric ($\text{Re}[n] > 1$ and $\text{Im}[n] \ll 1$) particles with subwavelength dimensions in all three directions are often called Mie resonances [65–67]. Recent works proved that halide perovskite nanoparticles can support Mie resonances in visible and near-infrared (IR) ranges [68–70]. Analytical calculations based on the Mie theory [71, 72] for a sphere with complex refractive index ($\text{Re}[n] = 2.5$ and $\text{Im}[n] = 0$) are shown in Figure 3A. The Mie theory gives the total scattering efficiencies upon irradiation of an incident plane wave:

$$C_{\text{scat}} = \frac{2\pi}{k^2} \sum_{j=1}^{\infty} (2j+1)(|a_j|^2 + |b_j|^2), \tag{8}$$

where $k = 2\pi n_h/\lambda$, n_h is the refractive index of the host media, λ is the incident wavelength. The coefficients a_j and b_j correspond to electric and magnetic scattering amplitudes for corresponding Mie modes (multipoles), which were actively studied during the last decade for various high-refractive-index materials (such as Si and GaAs).

The typical calculated scattered cross section for perovskite ($n = 2.5$) spherical nanoparticle is shown in Figure 3A. Black curve shows a total scattering cross section, color curve shows mode decomposition, dotted line shows eclectic-type modes (TE), and solid line shows magnetic-type modes (TM). For example, TM_1 corresponds to a magnetic dipole, TE_1 corresponds to electric dipole, TM_2 corresponds to magnetic quadrupole, TE_2 corresponds to electric quadrupole, and so on. In notation for TE, $\text{TM}_{i,m}$, m stands for the azimuthal mode number, and i stands for the radial mode number. This modeling provides important information on spectral width and overlapping between the Mie resonances. More detailed studies of the Mie resonances in halide perovskite nanoparticles were carried out recently both theoretically and experimentally [68, 69, 73, 74]. Remarkably, such spectral overlapping can result in specific modes interference and thus to control the directivity of emitted or scattered light [67, 75–77].

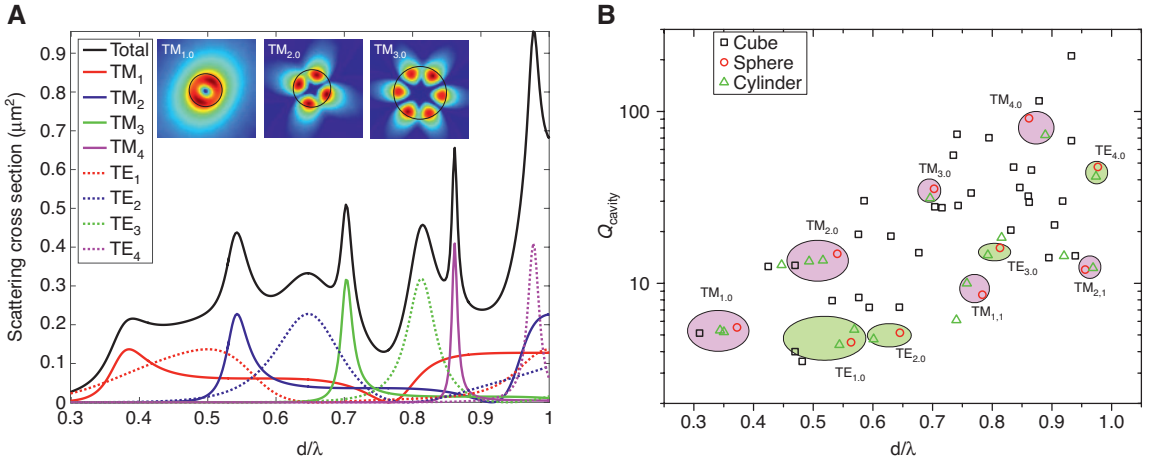

Figure 3: Resonant properties of halide perovskite cavities.
(A) Analytically calculated dependence of scattering cross section with mode decomposition for a sphere with refractive index $n = 2.5$ on the ratio of the particle diameter (d) and incident light wavelength (λ). Inset: electric field distributions for the modes $TM_{1,0}$ ($d/\lambda = 0.374$), $TM_{2,0}$ ($d/\lambda = 0.541$), $TM_{3,0}$ ($d/\lambda = 0.704$). (B) Numerically calculated dependence of Q factors for eigenmodes in the particles of three different shapes (spheres, cubes, and cylinders) on the ratio of diameter (or size for cubes) to wavelength. For cylinders, we consider height is equal to 200 nm.

More complicated numerical methods are required to solve the Maxwell equations for cylindrical, cubical, and other shapes of the nanoparticles. The Q_{cavity} factors of the eigenmodes in perovskite nanoparticles are calculated numerically by using finite-element method in an eigenmode solver in COMSOL Multiphysics. All calculations are carried out for single particles of three different shapes: cubes, spheres, and cylinders (height of cylinder considered permanent equal to 200 nm). Nanoresonators are considered in homogeneous environment with refractive index equal to one surrounded by perfectly matched layer imitating infinity space. The value for refractive index of particle is 2.5 that close to $CsPbBr_3$ thin film around its excitonic state. Figure 3B shows the dependence of eigenmode Q_{cavity} factors on cavity size. Color ovals show that modes near field distribution satisfy sphere multipole notation from Figure 3A. Insets show near-field distribution of electric field for the first magnetic modes. The considered shapes of perovskite nanoparticles can be fabricated by various methods [16, 17, 33, 78, 79], which will be discussed in the following sections in more detail.

3.2 Nanowires: Fabry–Perot resonances

One of the most popular shapes of nanocavities for perovskite single-particle lasers are nanowires (NWs), which are just prolonged nanoparticles in one direction. Owing to high reflectivity on facets, perovskite NW can be considered as a Fabry–Perot (F-P) resonator, whose Q_{cavity} factor is proportional to its length [80].

$$Q_{FP} = -\frac{Lk_{||}}{\ln|R_1R_2|}, \tag{9}$$

where R_1 and R_2 are the reflection coefficients at each facet, L is the nanowire length, and $k_{||}$ is the longitudinal projection of wavenumber along the NW axis.

Remarkably, F-P modes can interfere with Mie-like modes in NWs, resulting in Fano-like features in spectral response [81, 82]. Nevertheless, linear dependence of Q_{cavity} factor on length in NWs might be slower than that for Mie modes increasing in all three dimensions (Figure 3B). Thus, NWs usually do not show record-small volumes of perovskite-based nanolasers, except their integration with metal surfaces [83] or nanostructures [84].

In general, there are many approaches to synthesize perovskite 1D structures, but here we focus only on some of them yielding high-quality monocrystalline F-P cavities. The first one is conventional chemical vapor deposition (CVD) technique, which is widely exploited for the growth of inorganic nanowires and microwires from different materials such as ZnO, GaAs, InP, and so on. As CVD is a high-temperature process, it was found to produce various $CsPbX_3$ NWs possessing a cubic crystal phase. These NWs have rectangular or triangular cross section depending on the direction of growth (in plane or bottom-up) and crystal lattice parameters of the substrate

material (Si [13], mica [85, 86], Al_2O_3 [87]) or perovskite. In the case of lattice parameter inconsistency or utilization of a substrate with an amorphous top layer (for instance Si/SiO_2), the area of NW cross section could be different along the crystal growth direction [57]. The second is very similar to CVD, but a bit simpler approach to fabricate inorganic perovskite nanolasers was demonstrated by Wang et al. [88]. The authors showed that the temperature difference between substrate covered with a perovskite thin film and mica substrate triggers controlled growth of triangular NWs on the latter in air.

The shape and area of the NW cross section affect the confinement factor (η), which is supposed to be maximal for the low threshold lasing and can be expressed as follows [27]:

$$\eta = \frac{n_g}{n_b}\eta_0, \tag{10}$$

where n_b is the background refractive index, n_g is group velocity refractive index, and η_0 is a ratio of the energy in the active region to the energy in the entire waveguide and takes values smaller than 1. Therefore, in perovskite NWs, η can be larger than 1 as it is mostly influenced by high group refractive index, which is in the range of 5–17 [13, 57, 89]. In turn, the width and height of the most compact laser design based on NW should fall within a specific range to enable efficient propagation of the first fundamental electromagnetic mode along the resonator as well as to avoid competition between this mode and the other ones. For example, the optimal width and height of rectangular $MAPbI_3$ NWs, supporting TE-like fundamental mode ($\lambda = 787$ nm) having a minor longitudinal component, were calculated to be around 600 and 300 nm, respectively [57], whereas almost two times smaller dimensions were reported for $CsPbX_3$ nanolasers generating visible light [13].

In contrast to the vapor deposition techniques, wet chemical approaches employ the processes occurring at moderate temperature and resulting in the formation of tetragonal or orthorhombic perovskite structures. Therefore, NWs have only a rectangular cross section. The early reports on their slow solution growth describe bottom-up crystallization from lead halide or acetate films immersed in alcohol containing methylammonium or cesium halides [15, 90]. Then, synthesis was expanded to antisolvent diffusion method [91] and ligand-assisted reactions in which ionic organic species passivate certain crystallographic planes and invoke unidirectional crystallization [50, 89]. It should be pointed out that Q factors of the F-P resonators obtained by the wet chemical approaches are comparable or even better than those of NWs grown by CVD. In particular, recently, we have developed a few-minute synthesis of $CsPbBr_3$ NWs with truncated pyramidal end facets, which according to numerical calculations trap confined light in the vicinity of the very end of the cavity and decrease the out-coupling efficiency [89]. Moreover, ligand-assisted strategy successfully applied for the production of monodisperse quantum dots [92] is supposed to accelerate the development of technology, which will afford manufacturing of perovskite NWs having optimized dimensions for high-quality lasing.

3.3 Plates and disks: whispering gallery modes

When two characteristic lateral dimensions of a perovskite particle are larger than the emitted wavelength, and the thickness is subwavelength only, the structures are often called microplates (MPLs) or microdisks (MDs). These types of cavity support so-called whispering gallery modes (WGMs). Q_{cavity} factor of WGM in an MPL resonator with polygon shape is given as follows [93]:

$$Q_{\text{WGM}} = \frac{\pi d N n R^{\frac{N}{4}}}{2\lambda\left(1-R^{\frac{N}{2}}\right)}\sin\left(\frac{2\pi}{N}\right), \tag{11}$$

where d is the diameter of the circle that circumscribes the polygon, n is refractive index, N is the number of facets ($N > 2$), and R is reflection on the boundaries. For an ideal spherical resonator, Q_{cavity} factor is given by the following formula:

$$Q_{\text{WGM}}^{TE} = \frac{q\chi_i^2(q)(n^2-1)}{2} \tag{12}$$

$$Q_{\text{WGM}}^{TM} = \frac{q\chi_i^2(q)(n^2-1)}{2}\left(\frac{i(i+1)}{n^2q^2} + \frac{\chi_i'^2(q)}{\chi_i^2(q)}\right), \tag{13}$$

where i is radial mode number, $q = 2\pi d/\lambda$ where d is sphere diameter, and $\chi_i(q) = qy_i(q)$ is Riccati–Bessel functions, where $y_i(q)$ is Neumann functions.

Generally, spherical microparticles or MDs are more preferable as compared with cubic ones when the size is larger than the operating wavelength in free space, i.e. when there is an increase of incidence angle of WGM to the spherical boundary of particle, whereas this angle is fixed for the increasing polygon particles. However, a spherical shape does not correspond to any single-crystal state being likely an amorphous or polycrystalline one,

where defect concentration (N_T) is usually much higher as compared with single-crystal perovskites.

Among the regular shapes of perovskite plates supporting high-quality WGM regime, only three are possible: triangular, rectangular, and hexagonal because of perovskite crystal phases dictating the geometric parameters of the polygons. Rectangular cavities adopting cubic or orthorhombic crystal lattice can be grown by using the same approaches mentioned above for perovskite NWs [12, 50, 94]. Triangular and hexagonal plates have been reported only for $MAPbI_3$ and its mixed halide counterparts – $MAPbI_{3-x}Br_x$ and $MAPbI_{3-x}Cl_x$ with $x \ll 1$ [8]. These structures possess a tetragonal phase and can be fabricated by vapor deposition of lead halides crystallizing in the form of thin triangles or hexagons on mica followed by their thermal intercalation with methylammonium iodide. As compared to NWs of similar chemical composition, $MAPbI_3$ hexagonal MPLs exhibit much higher optical gain that allows reducing their lasing cutoff thickness down to 70 nm at room temperature [8].

Thin WGM cavities with a circular shape cannot be achieved either by CVD or by simple wet chemical approaches. Usually, their manufacturing is a complicated multistep process comprising growth of single-crystal perovskite MPLs or deposition of polycrystalline thin films that are accompanied by top-down lithography [95–97] or laser printing procedure [79, 98]. Thereby, when material losses ($1/Q_{abs}$) are compensated by pump and mode leakage losses ($1/Q_{leak}$) are extremely small, Q_{cavity} suffers mostly from both the sidewall roughness and polycrystallinity involved in the scattering losses (Q_{scat}) owing to technological reasons. Thus, in the following formula [99]:

$$\frac{1}{Q_{cavity}} = \frac{1}{Q_{abs}} + \frac{1}{Q_{leak}} + \frac{1}{Q_{scat}}. \tag{14}$$

the first two terms can become almost negligible as compared with the scattering losses. For example, in MD cavities, the losses caused by scattering on sidewall roughness (Q_{scat}) can be expressed as follows [100]:

$$Q_{scat} = \frac{3\lambda^3}{16\pi^{5/2}(n^2-1)} \frac{d/h}{L_c \xi^2}, \tag{15}$$

where d is MD diameter, h is MD thickness, and L_c and ξ are the roughness correlation length and amplitude, respectively.

Among different types of perovskite WGM resonators, the highest Q_{cavity} factors belong to spherical ones manufactured by CVD [16, 78, 101] and deposition of perovskite precursors or as-prepared quantum dots onto SiO_2 microspheres [23, 102]. Although CVD-grown $CsPbX_3$ spheres adopt an orthorhombic phase, which is supposed to crystallize in the form of cubes or bricks, the activation of surface tension forces at high temperature leads to the formation of spherical cavities [16, 78].

4 Experimental demonstrations of single-particle lasers: comparative analysis

Because of high optical losses at emission wavelengths of the halide perovskites, it is difficult to characterize Q_{cavity} factors of the nonexcited cavities. On the other hand, one can easily measure spectral width of the lasing modes above the threshold. The connection between Q_{cavity} factor of cavity and spectral width of the lasing mode was established by Lax [103] correcting the famous Schawlow–Townes equation:

$$\Delta\omega_{laser} = \frac{\pi\hbar\omega(\Delta\omega_{cavity})^2}{P_{out}}, \tag{16}$$

which can be presented as

$$Q_{laser} = \frac{\omega}{\Delta\omega_{laser}} = \frac{P_{out}Q_{cavity}^2}{\pi\hbar\omega^2}, \tag{17}$$

where ω is the radial frequency of the resonant mode, $\Delta\omega_{laser}$ and $\Delta\omega_{cavity}$ are the full width at half-maximum of the laser line and the resonance mode in cavity, respectively; P_{out} is the laser output power; and $\hbar$ is the Plank constant. This relation shows that laser spectral width above the lasing threshold is always narrower than the spectral width of the cavity mode and additionally depends on gain saturation. Thus, the comparison of laser quality factors (Q_{laser}) for various perovskite lasers measured from PL spectral above the lasing threshold should take into account properties of cavity and material properties.

Discussing the most optimal shapes of single-particle perovskite lasers, it should be stressed that each of them has some advantages and disadvantages. A spherical cavity has higher quality factor and vanishing contact area with substrate resulting in the reduction of mode leakage. On the contrary, small spherical particle is polycrystalline; i.e. it has high crystal lattice defect concentration. In turn, nanocubes, nanowires, and nanoplates have low defect concentration because these objects correspond to regular shapes, which are natural for single crystals. However, their disadvantage is higher mode leakage

to substrate and additional scattering on the sharp edges. Cylindrical particles require lithographic methods of fabrication, which usually generate additional defects in perovskite material owing to overheating, amorphization, or spoiling by etching gas/liquid.

Besides the leakage losses, strong impact on Q_{laser} has the scattering ones originating from low volume integrity of the cavity and its surface roughness. In particular, it was shown that single-crystal $MAPbBr_3$ MDs having sidewall roughness less than 5 nm support lasing with Q_{laser} up to 6000 [95], whereas polycrystalline $MAPbI_3$ cavities with more rough sidewall (>8 nm) fabricated by chemical etching through a mask yield lasing with Q_{laser} up to 710 [97]. On the other hand, recently, it was demonstrated how the roughness can be exploited to support a single mode lasing in $MAPbX_3$ ($X = I$, $Br_{0.33}I_{0.66}$, Br) MDs printed by means of laser ablation technique [79]. When the roughness is close to 50 nm, the WGM cavity with diameter from 2 to 5 μm enters into chaotic operation regime where predominantly only one lasing mode with $Q_{laser} \approx 5000$ survives.

Among the numerous results on lasing in perovskite single-particle structures presented in literature since 2014, we would like to point out the outstanding ones in our opinion: (i) the smallest NW supporting lasing at F-P resonances with $Q_{laser} \approx 6000$ at temperature 4 K (Figure 4A) [104]; (ii) the smallest perovskite laser ever – Mie-resonant nanocube with ≈420-nm edge size and showing $Q_{laser} = 670$ (Figure 4B) [33]; (iii) spherical WGM microcavity demonstrating the highest Q_{laser} ever – 15,000 (Figure 4C) among perovskite lasers [78].

As many factors affect the lasing properties of nanocavities and microcavities, some figure of merit is required to compare them to each other. As a reasonable criterion, we propose a dependence of Q_{laser} on volume (V) of

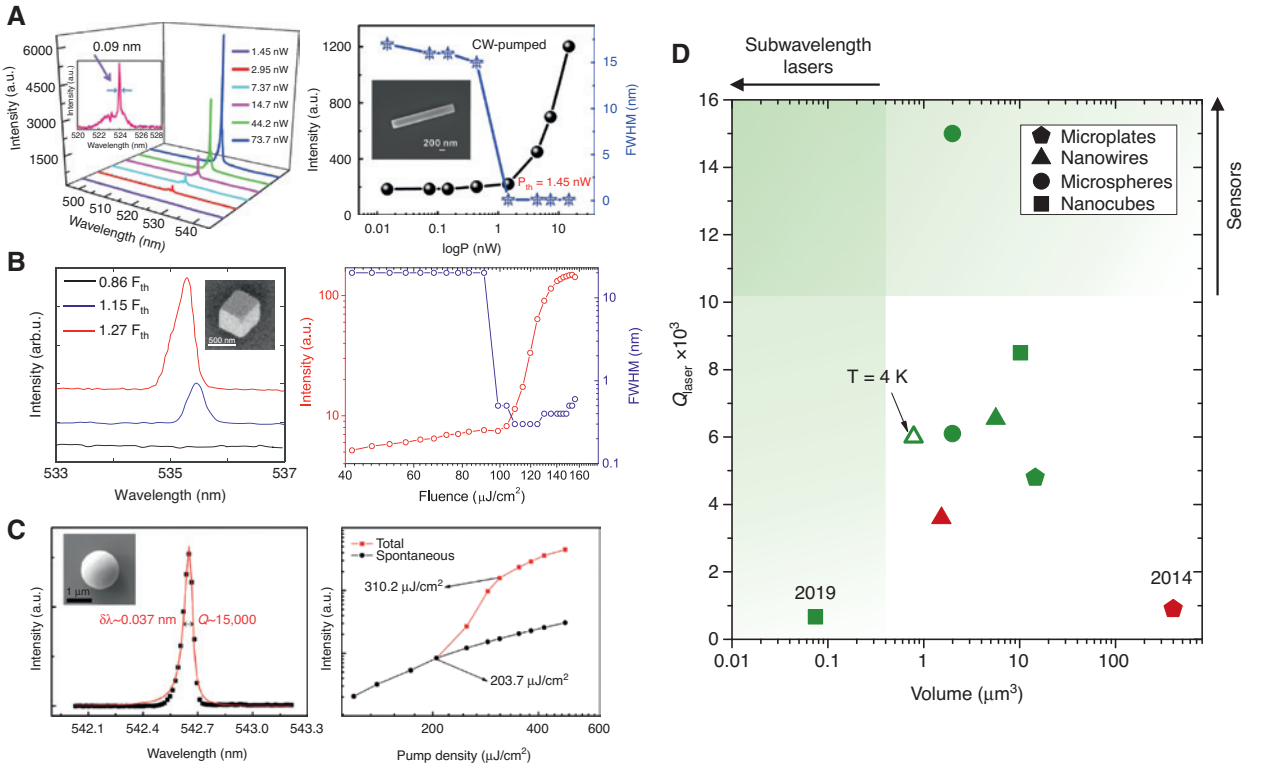

Figure 4: Experimental demonstration of single-particle lasers.
(A) The fluence dependence of continuous wave (CW) pumped lasing spectra from a single $CsPbBr_3$ NW at helium temperature (left) and fluence dependence of CW pumped lasing intensity (blue) and full width on half maximum (FWHM) (black) from a single $CsPbBr_3$ NW (right), indicating a low threshold of 1.45 nW and high Q factor around 6000. (B) Pump intensity-dependent emission spectra at different values of fluence below and above the lasing threshold (left) for 480-nm nanocube laser and output emission intensity (red) and emission FWHM (blue) as a function of pump fluence (right). (C) Integrated emission intensity as a function of pump fluence showing the lasing threshold around 200 μJ/cm² (left) and Lorentz fitting of a lasing oscillation mode at 542.6 nm (right), giving an ultrasmall line width of 0.037 nm, corresponding to an ultrahigh Q factor around 15,000. (D) Experimental values of lasing mode quality factors for different perovskite lasers of different shapes (microplates [8, 94], nanowires [15, 89, 104], microspheres [16, 78], and nanocube [17, 33]) vs. volume. The colors of sign show the color of laser: green: 500–550 nm, red: 690–780 nm.

a single-particle perovskite laser (Figure 4D), resembling the calculated dependence of Q_{cavity} on cavity size. Indeed, the results in Figure 3B help to predict a general trend for the experimentally observed $Q_{laser}(V)$ values. In particular, it seems to be challenging to achieve $Q_{laser} > 10{,}000$ for the volumes $V < 1\ \mu m^3$, because high-quality laser has to compromise on compact dimensions.

Achievement of high Q_{laser} from single-particle resonators makes it possible to design optical sensors capable of detection of various analytes at ultralow concentrations. Usually, the higher the Q factor, the higher the sensitivity of a laser to changes of any external parameters [105]. Another important application is photonic integrated circuit consisting of high-quality ultracompact nanolasers integrated with complementary metal-oxide-semiconductor technology compatible waveguides. In particular, it can be applied for a high-speed multichannel coherent transmitter [106] operating at extremely low spacing between channels. In this regard, perovskites are promising materials because they are tunable, cheap, and easily compatible with silicon-based materials and designs. Also, the lasers with higher Q_{cavity} factors operate at lower pump fluence, which should help to substantially increase their long-term stability.

5 Conclusion and outlook

To summarize, the application of the halide perovskites has evolved from a simple synthesis optimization (XIX century) to the fabrication of advanced nanophotonic designs allowing for lasing at the deeply subwavelength scale (XXI century). By now, current understanding of nanocavity and material properties, as well as available advanced methods of nanofabrication of perovskite-based designs, allowed to realize the compact and efficient subwavelength lasers. For example, recent experimental results demonstrated that Mie-resonant nanocubes $CsPbBr_3$ nanoparticles with high crystalline quality are the smallest designs among those reported so far. Moreover, these particles have sizes comparable to or smaller than the cavities based on GaN [107, 108], InGaP [109], and CdSe [110]. Also, nanolasers made of halide perovskites with high multiphoton photoexcitation efficiency would allow working in deeply subwavelength regime relative to the pumping wavelengths, being useful for various upconversion applications [111].

Nevertheless, there are many challenges to solve. First, electrically driven perovskite nanolasers are still not realized, owing to low thermal conductivity (<10 $W/m \cdot K$) [43] of the halide perovskites resulting in their overheating at high current densities. This problem requires further lowering of lasing threshold via optimization of the material properties (e.g. defects concentration) and maximizing Q factor of the nanocavity. Importantly, both improvement of thermal sink and Q factor can be achieved via proper substrate engineering, which is definitely a topic of further studies. The second problem is the control of wavelength of stimulated emission from perovskite nanolasers. In principle, anion exchange reaction allowed to demonstrate a broad range of colors from blue to near-IR range. However, stability and QY of the mixed-anion nanolasers always get worse. To solve this problem, smart postprocessing is required for defect healing and phase stabilization. The third problem is the integration of the nanolasers with advanced optical elements for further waveguiding and signal processing. In this way, nanoantenna-like effects related to interference of resonances in subwavelength cavities could improve out-coupling efficiency and directivity for the emitted light.

Acknowledgments: We are thankful to Kirill Koshelev, Prof. Sergei Kulinich, and Prof. Yuri Kivshar for the useful discussions. This work was partially supported by Russian Science Foundation (17-73-20336). E.Y.T. acknowledges the Russian Science Foundation (19-19-00177, Funder Id: http://dx.doi.org/10.13039/501100006769) supporting numerical simulations and the Russian Federation President Scholarship for Young Scientists.

References

[1] Wells HL. Art. xvi.–on the coesium-and the potassium-lead halides. Am J Sci 1893;45:121.
[2] Weber D. $CH_3NH_3PBX_3$, ein Pb(II)-system mit kubischer perowskitstruktur/$CH_3NH_3PBX_3$, a Pb(II)-system with cubic perovskite structure. Z Naturforsch B 1978;33:1443–5.
[3] Kojima A, Teshima K, Shirai Y, Miyasaka T. Organometal halide perovskites as visible-light sensitizers for photovoltaic cells. J Am Chem Soc 2009;131:6050–1.
[4] Xing G, Mathews N, Lim SS, et al. Low-temperature solution-processed wavelength-tunable perovskites for lasing. Nat Mater 2014;13:476–80.
[5] Jia Y, Kerner RA, Grede AJ, Rand BP, Giebink NC. Continuous-wave lasing in an organic–inorganic lead halide perovskite semiconductor. Nat Photonics 2017;11:784.
[6] Maiman T. Stimulated optical radiation in ruby. Nature 1960;187:493.
[7] Alferov ZI. Alas-GaAs heterojunction injection lasers with a low room-temperature threshold. Sov Phys Semicond 1970;3:1107–10.
[8] Zhang Q, Ha ST, Liu X, Sum TC, Xiong Q. Room-temperature near-infrared high-Q perovskite whispering-gallery planar nanolasers. Nano Lett 2014;14:5995–6001.

[9] Møller CK. Crystal structure and photoconductivity of caesium plumbohalides. Nature 1958;182:1436.
[10] Kagan C, Mitzi D, Dimitrakopoulos C. Organic–inorganic hybrid materials as semiconducting channels in thin-film field-effect transistors. Science 1999;286:945–7.
[11] Dohner ER, Hoke ET, Karunadasa HI. Self-assembly of broadband white-light emitters. J Am Chem Soc 2014;136:1718–21.
[12] Liao Q, Hu K, Zhang H, Wang X, Yao J, Fu H. Perovskite microdisk microlasers self-assembled from solution. Adv Mater 2015;27:3405–10.
[13] Park K, Lee JW, Kim JD, et al. Light–matter interactions in cesium lead halide perovskite nanowire lasers. J Phys Chem Lett 2016;7:3703–10.
[14] Zhang H, Liao Q, Wu Y, et al. 2D Ruddlesden–Popper perovskites microring laser array. Adv Mater 2018;30:1706186.
[15] Zhu H, Fu Y, Meng F, et al. Lead halide perovskite nanowire lasers with low lasing thresholds and high quality factors. Nat Mater 2015;14:636.
[16] Tang B, Dong H, Sun L, et al. Single-mode lasers based on cesium lead halide perovskite submicron spheres. ACS Nano 2017;11:10681–8.
[17] Zhou B, Dong H, Jiang M, et al. Single-mode lasing and 3D confinement from perovskite micro-cubic cavity. J Mater Chem C 2018;6:11740–8.
[18] Mitzi DB. Synthesis, structure, and properties of organic–inorganic perovskites and related materials. Prog Inorg Chem 1999:1–121.
[19] Mizusaki J, Arai K, Fueki K. Ionic conduction of the perovskite-type halides. Solid State Ion 1983;11:203–11.
[20] Knop O, Wasylishen RE, White MA, Cameron TS, Oort MJV. Alkylammonium lead halides. Part 2. $CH_3NH_3PbX_3$ (X=Cl, Br, I) perovskites: cuboctahedral halide cages with isotropic cation reorientation. Can J Chem 1990;68:412–22.
[21] Snaith HJ. Present status and future prospects of perovskite photovoltaics. Nat Mater 2018;17:372.
[22] Lu M, Zhang Y, Wang S, Guo J, Yu WW, Rogach AL. Metal halide perovskite light-emitting devices: promising technology for next-generation displays. Adv Funct Mater 2019;29:1902008.
[23] Sutherland BR, Hoogland S, Adachi MM, Wong CT, Sargent EH. Conformal organohalide perovskites enable lasing on spherical resonators. ACS Nano 2014;8:10947–52.
[24] McCall S, Levi A, Slusher R, Pearton S, Logan R. Whispering-gallery mode microdisk lasers. Appl Phys Lett 1992;60:289–91.
[25] Ledentsov NN, Grundmann M, Heinrichsdorff F, et al. Quantum-dot heterostructure lasers. IEEE J Sel Top Quantum Electron 2000;6:439–51.
[26] Koyama F. Recent advances of vcsel photonics. J Lightwave Technol 2006;24:4502–513.
[27] Ning C-Z. Semiconductor nanolasers. Phys Status Solidi (B) 2010;247:774–88.
[28] Ding K, Ning C-Z. Fabrication challenges of electrical injection metallic cavity semiconductor nanolasers. Semicond Sci Technol 2013;28:124002.
[29] Eaton SW, Fu A, Wong AB, Ning C-Z, Yang P. Semiconductor nanowire lasers. Nat Rev Mater 2016;1:16028.
[30] Gu Q, Fainman Y. Semiconductor nanolasers. Cambridge, UK: Cambridge University Press, 2017.
[31] Ma R-M, Oulton RF. Applications of nanolasers. Nat Nanotechnol 2019;14:12–22.
[32] Ning C-Z. Semiconductor nanolasers and the size-energy-efficiency challenge: a review. Adv Photonics 2019;1:014002.
[33] Tiguntseva EY, Koshelev KL, Furasova AD, et al. Single-particle Mie-resonant all-dielectric nanolasers. 2019, arXiv preprint arXiv:1905.08646.
[34] Sutherland BR, Hoogland S, Adachi MM, et al. Perovskite thin films via atomic layer deposition. Adv Mater 2015;27:53–8.
[35] Zheng K, Zhu Q, Abdellah M, et al. Exciton binding energy and the nature of emissive states in organometal halide perovskites. J Phys Chem Lett 2015;6:2969–75.
[36] Yang Y, Yang M, Li Z, Crisp R, Zhu K, Beard MC. Comparison of recombination dynamics in $CH_3NH_3PbBr_3$ and $CH_3NH_3PbI_3$ perovskite films: influence of exciton binding energy. J Phys Chem Lett 2015;6:4688–92.
[37] Kunugita H, Hashimoto T, Kiyota Y, et al. Excitonic feature in hybrid perovskite $CH_3NH_3PbBr_3$ single crystals. Chem Lett 2015;44:852–4.
[38] Miyata A, Mitioglu A, Plochocka P, et al. Direct measurement of the exciton binding energy and effective masses for charge carriers in organic–inorganic tri-halide perovskites. Nat Phys 2015;11:582–7.
[39] Yamada T, Aharen T, Kanemitsu Y. Near-band-edge optical responses of $CH_3NH_3PbCl_3$ single crystals: photon recycling of excitonic luminescence. Phys Rev Lett 2018;120:057404.
[40] Jiang Y, Wang X, Pan A. Properties of excitons and photogenerated charge carriers in metal halide perovskites. Adv Mater 2019:1806671.
[41] Mosconi E, Meggiolaro D, Snaith HJ, Stranks SD, De Angelis F. Light-induced annihilation of Frenkel defects in organo-lead halide perovskites. Energy Environ Sci 2016;9:3180–7.
[42] Stranks SD, Snaith HJ. Metal-halide perovskites for photovoltaic and light-emitting devices. Nat Nanotechnol 2015;10:391.
[43] Sutherland BR, Sargent EH. Perovskite photonic sources. Nat Photonics 2016;10:295.
[44] Jeon NJ, Noh JH, Kim YC, Yang WS, Ryu S, Seok SI. Solvent engineering for high-performance inorganic–organic hybrid perovskite solar cells. Nat Mater 2014;13:897.
[45] Clark D, Stoumpos C, Saouma F, Kanatzidis M, Jang J. Polarization-selective three-photon absorption and subsequent photoluminescence in $CsPbBr_3$ single crystal at room temperature. Phys Rev B 2016;93:195202.
[46] Liu Z, Yang J, Du J, et al. Robust subwavelength single-mode perovskite nanocuboid laser. ACS Nano 2018;12:5923–31.
[47] Hurlbut WC, Lee Y-S, Vodopyanov K, Kuo P, Fejer M. Multiphoton absorption and nonlinear refraction of GaAs in the mid-infrared. Opt Lett 2007;32:668–70.
[48] Streltsov AM, Moll K, Gaeta AL, Kung P, Walker D, Razeghi M. Pulse autocorrelation measurements based on two-and three-photon conductivity in a GaN photodiode. Appl Phys Lett 1999;75:3778–80.
[49] Gu Z, Wang K, Sun W, et al. Two-photon pumped $CH_3NH_3PbBr_3$ perovskite microwire lasers. Adv Opt Mater 2016;4:472–9.
[50] Zhang W, Peng L, Liu J, et al. Controlling the cavity structures of two-photon-pumped perovskite microlasers. Adv Mater 2016;28:4040–6.
[51] Wang X, Zhou H, Yuan S, et al. Cesium lead halide perovskite triangular nanorods as high-gain medium and effective cavities for multiphoton-pumped lasing. Nano Res 2017;10:3385–95.

[52] Qian X, Gu X, Yang R. Lattice thermal conductivity of organic–inorganic hybrid perovskite $CH_3NH_3PbI_3$. Appl Phys Lett 2016;108:063902.
[53] Jia Y, Kerner RA, Grede AJ, Rand BP, Giebink NC. Factors that limit continuous-wave lasing in hybrid perovskite semiconductors. Adv Opt Mater 2019, https://doi.org/10.1002/adom.201901514.
[54] Stranks SD, Burlakov VM, Leijtens T, Ball JM, Goriely A, Snaith HJ. Recombination kinetics in organic–inorganic perovskites: excitons, free charge, and subgap states. Phys Rev Appl 2014;2:034007.
[55] deQuilettes DW, Frohna K, Emin D, et al. Charge-carrier recombination in halide perovskites. Chem Rev 2019;119:11007–19.
[56] Liashenko TG, Cherotchenko ED, Pushkarev AP, et al. Electronic structure of $CsPbBr_{3-x}CL_x$ perovskites: synthesis, experimental characterization, and DFT simulations. Phys Chem Chem Phys 2019;21:18930–8.
[57] Zhou H, Yuan S, Wang X, et al. Vapor growth and tunable lasing of band gap engineered cesium lead halide perovskite micro/nanorods with triangular cross section. ACS Nano 2016;11:1189–95.
[58] Ruf F, Aygüler MF, Giesbrecht N, et al. Temperature-dependent studies of exciton binding energy and phase-transition suppression in (Cs, FA, MA) Pb (I, Br)$_3$ perovskites. APL Mater 2019;7:031113.
[59] Casey HJ. Heterostructure lasers. Amsterdam, the Netherlands, Elsevier, 2012.
[60] Coleman JJ, Young JD, Garg A. Semiconductor quantum dot lasers: a tutorial. J Lightwave Technol 2010;29:499–510.
[61] Schlaus AP, Spencer MS, Miyata K, et al. How lasing happens in $CsPbBr_3$ perovskite nanowires. Nat Commun 2019;10:265.
[62] Shang Q, Zhang S, Liu Z, et al. Surface plasmon enhanced strong exciton–photon coupling in hybrid inorganic–organic perovskite nanowires. Nano Lett 2018;18:3335–43.
[63] Du W, Zhang S, Zhang Q, Liu X. Recent progress of strong exciton–photon coupling in lead halide perovskites. Adv Mater 2018:1804894.
[64] Schlaus AP, Spencer MS, Zhu X. Light–matter interaction and lasing in lead halide perovskites. Acc Chem Res 2019;52:2950–9.
[65] Kuznetsov AI, Miroshnichenko AE, Fu YH, Zhang J, Luk'yanchuk B. Magnetic light. Sci Rep 2012;2:492.
[66] Krasnok A, Makarov S, Petrov M, Savelev R, Belov P, Kivshar Y. Towards all-dielectric metamaterials and nanophotonics. In: Metamaterials X, Vol. 9502:950203. Bellingham, WA, USA, International Society for Optics and Photonics; 2015.
[67] Kuznetsov AI, Miroshnichenko AE, Brongersma ML, Kivshar YS, Luk'yanchuk B. Optically resonant dielectric nanostructures. Science 2016;354:aag2472.
[68] Tiguntseva E, Zograf GP, Komissarenko FE, et al. Light-emitting halide perovskite nanoantennas. Nano Lett 2018;18:1185–90.
[69] Tiguntseva EY, Baranov DG, Pushkarev AP, et al. Tunable hybrid Fano resonances in halide perovskite nanoparticles. Nano Lett 2018;18:5522–9.
[70] Berestennikov AS, Voroshilov PM, Makarov SV, Kivshar YS. Active meta-optics and nanophotonics with halide perovskites. Appl Phys Rev 2019;6:031307.
[71] Mie G. Beiträge zur optik trüber medien, speziell kolloidaler metallösungen. Ann Phys 1908;330:377–445.
[72] Bohren CF, Huffman DR. Absorption and scattering of light by small particles. Hoboken, NJ, USA, John Wiley & Sons, 2008.
[73] Berestennikov A, Li Y, Iorsh I, Zakhidov AA, Rogach A, Makarov S. Beyond quantum confinement: excitonic nonlocality in halide perovskite nanoparticles with Mie resonances. Nanoscale 2019;11:6747–54.
[74] Tonkaev P, Zograf G, Makarov S. Optical cooling of lead halide perovskite nanoparticles enhanced by Mie resonances. Nanoscale 2019;11:17800–6.
[75] Staude I, Miroshnichenko AE, Decker M, et al. Tailoring directional scattering through magnetic and electric resonances in subwavelength silicon nanodisks. ACS Nano 2013;7:7824–32.
[76] Makarov S, Kudryashov S, Mukhin I, et al. Tuning of magnetic optical response in a dielectric nanoparticle by ultrafast photoexcitation of dense electron–hole plasma. Nano Lett 2015;15:6187–92.
[77] Makarov SV, Zalogina AS, Tajik M, et al. Light-induced tuning and reconfiguration of nanophotonic structures. Laser Photonics Rev 2017;11:1700108.
[78] Tang B, Sun L, Zheng W, et al. Ultrahigh quality upconverted single-mode lasing in cesium lead bromide spherical microcavity. Adv Opt Mater 2018;6:1800391.
[79] Zhizhchenko A, Syubaev S, Berestennikov A, et al. Single-mode lasing from imprinted halide-perovskite microdisks. ACS Nano 2019;13:4140–7.
[80] Maslov AV, Ning CZ. Reflection of guided modes in a semiconductor nanowire laser. Appl Phys Lett 2003;83:1237–9.
[81] Landreman PE, Chalabi H, Park J, Brongersma ML. Fabry–Perot description for Mie resonances of rectangular dielectric nanowire optical resonators. Opt Express 2016;24:29760–72.
[82] Yang Y, Miroshnichenko AE, Kostinski SV, et al. Multimode directionality in all-dielectric metasurfaces. Phys Rev B 2017;95:165426.
[83] Oulton RF, Sorger VJ, Zentgraf T, et al. Plasmon lasers at deep subwavelength scale. Nature 2009;461:629.
[84] Li YJ, Lv Y, Zou C-L, Zhang W, Yao J, Zhao YS. Output coupling of perovskite lasers from embedded nanoscale plasmonic waveguides. J Am Chem Soc 2016;138:2122–5.
[85] Huang L, Gao Q, Sun L-D, et al. Composition-graded cesium lead halide perovskite nanowires with tunable dual-color lasing performance. Adv Mater 2018;30:1800596.
[86] Chen J, Fu Y, Samad L, et al. Vapor-phase epitaxial growth of aligned nanowire networks of cesium lead halide perovskites ($CsPbX_3$, X=Cl, Br, I). Nano Lett 2016;17:460–6.
[87] Wang X, Shoaib M, Wang X, et al. High-quality in-plane aligned $CsPbX_3$ perovskite nanowire lasers with composition dependent strong exciton–photon coupling. ACS Nano 2018, https://doi.10.1021/acsnano.8b02793.
[88] Wang Y, Yasar M, Luo Z, et al. Temperature difference triggering controlled growth of all-inorganic perovskite nanowire arrays in air. Small 2018;14:1803010.
[89] Pushkarev AP, Korolev VI, Markina DI, et al. A few-minute synthesis of $CsPbBr_3$ nanolasers with a high quality factor by spraying at ambient conditions. ACS Appl Mater Interfaces 2018;11:1040–8.
[90] Eaton SW, Lai M, Gibson NA, et al. Lasing in robust cesium lead halide perovskite nanowires. Proc Natl Acad Sci 2016;113:1993–8.
[91] He X, Liu P, Wu S, Liao Q, Yao J, Fu H. Multi-color perovskite nanowire lasers through kinetically controlled solution growth followed by gas-phase halide exchange. J Mater Chem C 2017;5:12707–13.

[92] Zhang F, Zhong H, Chen C, et al. Brightly luminescent and color-tunable colloidal $CH_3NH_3PbX_3$ (X=Br, I, Cl) quantum dots: potential alternatives for display technology. ACS Nano 2015;9:4533–42.
[93] Liu L, Yao H, Li H, Wang Z, Shi Y. Recent advances of low-dimensional materials in lasing applications. FlatChem 2018;10:22–38.
[94] Zhang Q, Su R, Liu X, Xing J, Sum TC, Xiong Q. High-quality whispering-gallery-mode lasing from cesium lead halide perovskite nanoplatelets. Adv Funct Mater 2016;26:6238–45.
[95] Zhang N, Sun W, Rodrigues SP, et al. Highly reproducible organometallic halide perovskite microdevices based on top-down lithography. Adv Mater 2017;29:1606205.
[96] Wang S, Liu Y, Li G, et al. Lead halide perovskite based micro-disk lasers for on-chip integrated photonic circuits. Adv Opt Mater 2018;6:1701266.
[97] Cegielski PJ, Giesecke AL, Neutzner S, et al. Monolithically integrated perovskite semiconductor lasers on silicon photonic chips by scalable top-down fabrication. Nano Lett 2018;18:6915–23.
[98] Shishkin I, Polushkin A, Tiguntseva E, et al. Single-step direct laser writing of halide perovskite microlasers. Appl Phys Express 2019;12:122001.
[99] Slusher R, Levi A, Mohideen U, McCall S, Pearton S, Logan R. Threshold characteristics of semiconductor microdisk lasers. Appl Phys Lett 1993;63:1310–2.
[100] Borselli M, Johnson TJ, Painter O. Beyond the Rayleigh scattering limit in high-Q silicon microdisks: theory and experiment. Opt Express 2005;13:1515–30.
[101] Du W, Zhang S, Wu Z, et al. Unveiling lasing mechanism in $CsPbBr_3$ microsphere cavities. Nanoscale 2019;11:3145–53.
[102] Yakunin S, Protesescu L, Krieg F, et al. Low-threshold amplified spontaneous emission and lasing from colloidal nanocrystals of caesium lead halide perovskites. Nat Commun 2015;6:8056.
[103] Lax M. Classical noise. v. noise in self-sustained oscillators. Phys Rev 1967;160:290.
[104] Jiang L, Liu R, Su R, et al. Continuous wave pumped single-mode nanolasers in inorganic perovskites with robust stability and high quantum yield. Nanoscale 2018;10:13565–71.
[105] Vollmer F, Arnold S. Whispering-gallery-mode biosensing: label-free detection down to single molecules. Nat Methods 2008;5:591.
[106] Summers J, Vallaitis T, Evans P, et al. Monolithic InP-based coherent transmitter photonic integrated circuit with 2.25 Tbit/s capacity. Electron Lett 2014;50:1150–2.
[107] Lai C-M, Wu H-M, Huang P-C, Wang S-L, Peng L-H. Single mode stimulated emission from prismlike gallium nitride submicron cavities. Appl Phys Lett 2007;90:141106
[108] Gargas DJ, Moore MC, Ni A, et al. Whispering gallery mode lasing from zinc oxide hexagonal nanodisks. ACS Nano 2010;4:3270–6.
[109] Zhang Z, Yang L, Liu V, Hong T, Vahala K, Scherer A. Visible submicron microdisk lasers. Appl Phys Lett 2007;90:111119.
[110] Wang S, Wang X-Y, Li B, et al. Unusual scaling laws for plasmonic nanolasers beyond the diffraction limit. Nat Commun 2017;8:1889.
[111] Zhou J, Liu Q, Feng W, Sun Y, Li F. Upconversion luminescent materials: advances and applications. Chem Rev 2014;115:395–465.